remote sensing

MDPI

Article

Multipath Interferences in Ground-Based Radar Data: A Case Study

Célia Lucas [1,*], Silvan Leinss [1,*], Yves Bühler [2], Armando Marino [3] and Irena Hajnsek [1,4]

1 Institute of Environmental Engineering (IfU), ETH Zürich, 8093 Zürich, Switzerland; irena.hajnsek@dlr.de
2 Institute for Snow and Avalanche Research (SLF), 7260 Davos Dorf, Switzerland; buehler@slf.ch
3 Department of Engineering and Innovation, Open University, MK7 6AA Milton Keynes, UK; armando.marino@open.ac.uk
4 Microwaves and Radar Institute, German Aerospace Center (DLR), 82234 Weßling, Germany
* Correspondence: lucas@ifu.baug.ethz.ch (C.L.); leinss@ifu.baug.ethz.ch (S.L.); Tel.: +41-44-633-33-10 (C.L.); +41-44-633-40-45 (S.L.)

Received: 24 October 2017; Accepted: 2 December 2017; Published: 5 December 2017

Abstract: Multipath interference can occur in ground-based radar data acquired with systems with a large antenna beam width in elevation in an upward looking geometry, where the observation area and the radar are separated by a reflective surface. Radiation reflected at this surface forms a coherent overlay with the direct image of the observation area and appears as a fringe-like pattern in the data. This deteriorates the phase and intensity data and therefore can pose a considerable disadvantage to many ground-based radar measurement campaigns. This poses a problem for physical parameter retrieval from backscatter intensity and polarimetric data, absolute and relative calibration on corner reflectors, the generation of digital elevation models from interferograms and in the case of a variable reflective surface, differential interferometry. The main parameters controlling the interference pattern are the vertical distance between the radar antennas and the reflective surface, and the reflectivity of this surface. We used datasets acquired in two different locations under changing conditions as well as a model to constrain and fully understand the phenomenon. To avoid data deterioration in test sites prone to multipath interference, we tested a shielding of the antennas preventing the radar waves from illuminating the reflective surface. In our experiment, this strongly reduced but did not completely prevent the interference. We therefore recommend avoiding measurement geometries prone to multipath interferences.

Keywords: radar; interference; interferometry; reflection; multipath interference

1. Introduction

Ground-based radars increasingly gain importance in various geoscientific fields. With their ability to measure with a high temporal resolution in the order of minutes, they have a crucial advantage to satellite-borne radars, which have return times of several days. High measurement frequencies make ground-based radars ideal for the monitoring of fast moving and decorrelating surfaces. Many ground-based radar campaigns focus on the monitoring of regions prone to landslides and rockfall, e.g., [1–9]. Other geotechnical applications include the monitoring of slope instabilities in quarries and open pit mines [10,11]. In the cryospheric field, ground-based radar interferometry is widely used to determine for example the glacier surface velocity, e.g., [12,13], to detect changes in snow water equivalent [14], to identify wet snow avalanche precursors movements [15,16] or to map snow avalanches [17]. Various ground-based radars have also been used for the generation of digital elevation models (DEMs), e.g., [18,19]. In [20,21], reviews of recent ground-based radar systems and their applications are provided. Many of the aforementioned applications could be affected by multipath interferences (MPI) presented here if the measurements are performed in an unfortunate geometry.

Due to the wide range of applications where these findings may be of utmost importance, we aim to raise awareness of this problem in the ground-based radar community. With MPI, we describe the interference between the direct wave travelling between radar and target and an indirect wave reflected at a surface before reaching the target. This is analogous to Lloyd's mirror experiment [22]. To our knowledge, such interferences were so far never reported for ground-based imaging radar data. However, in other fields, multipath signals are explicitly exploited. An example of this are the sea interferometers in radio astronomy, invented in the 1940s [23]. In the field of flight tracking radars, the problem of multipath interference is already widely recognised and poses a considerable difficulty for tracking targets at low elevation angles, e.g., [24].

We observed the MPI most prominently in backscatter intensity data, but it also strongly affects single pass interferometric data and prevents accurate radar calibration. In the backscatter images, the MPI signal is clearly visible as intensity undulations following the topographic contours with a frequency depending on the local slope steepness. Similarly to contour lines, in steeper areas, the distance between the undulations is smaller than with flat terrain. A prominent example of the MPI pattern is shown in Figure 1, which is a backscatter intensity image acquired in the Davos test site, described in Section 1.2.1. In interferometric data, the multipath interferences appear as not fully developed fringes, i.e., phase undulations of less than 2 π cycles.

To understand the origin of the MPI pattern, the initial dataset, where we had noticed it first, was thoroughly analysed. Later, a second measurement campaign at a new test site, tailored to the investigation of the parameters influencing the MPI pattern appearance, intensity and frequency, was performed. Additionally, a model based on the 2 m digital elevation model swissALTI^{3D} provided by the Federal Office of Topography swisstopo was designed, reproducing the frequency, location and temporal evolution of multipath interferences in the geometry of the two test sites. We conclude by proposing potential solutions to reduce MPI in ground-based radar applications.

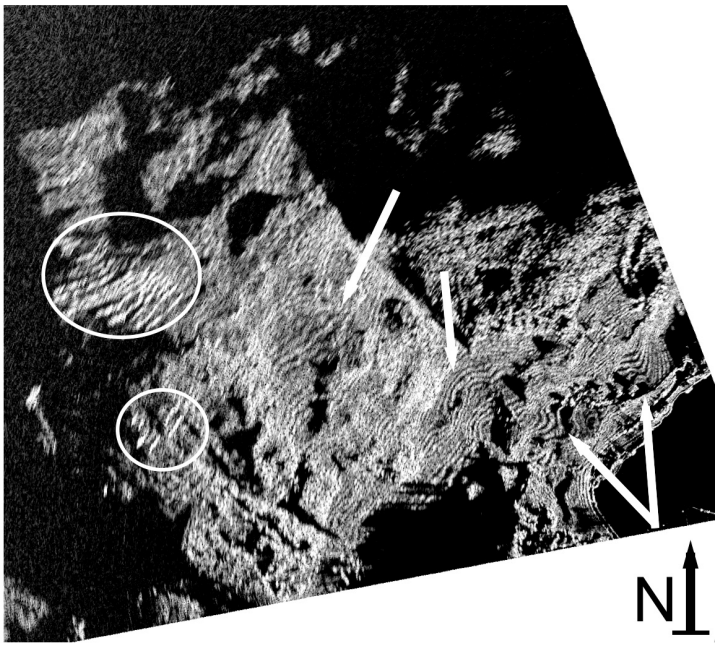

Figure 1. Backscatter intensity image showing multipath interference pattern as intensity undulations following the topography. Data was acquired in the Davos test site (Section 1.2.1) in VV polarisation on 1 October 2016. We performed temporal multilooking over 10 consecutive images acquired within 30 min to reduce speckle. Arrows point to the most prominent multipath interference features. Note that the bright features circled in white are avalanche protection structures that have a similar looking response.

1.1. KAPRI Instrument Details

The radar used in this study is a second generation GPRI (GAMMA Portable Radar Interferometer) [25] modified to have polarimetric capabilities by adding three horizontally polarised antennas. Our polarimetric GPRI [26] is called KAPRI (Ku-band Advanced Polarimetric Radar Interferometer).

KAPRI has six antennas, three vertically and three horizontally polarised. Each polarisation has one transmit and two receive antennas. This gives the system fully polarimetric and interferometric capabilities. It is a coherent, real aperture Frequency-Modulated Continuous Wave FMCW radar with the ability to scan up to 360° around its vertical center axis. The antennas are 2.06 m long slotted wave guide antennas with an azimuthal beamwidth of 0.385° and elevation beamwidth of 35°. Vertical baselines vary with the antenna arrangement but are limited by the antenna tower to B_{max} = 36 cm, corresponding to a height of ambiguity (HoA) of 52 m at a range distance of 1 km, assuming an incidence angle of 70°, which is typical for an upward looking geometry. The parameters are summarised in Table 1.

Table 1. Ku-band Advanced Polarimetric Radar Interferometer system parameters.

Parameter	Value	Unit
center frequency: f_c	17.2	GHz
bandwidth: Bw	200	MHz
azimuth beamwidth	0.385	deg
elevation beamwidth	35	deg
range resolution: δ_r	0.75	m
δ_{az} at 1 km range distance	7.0	m
δ_{az} at 2 km range distance	14.0	m
polarisation	HH, VV, HV, VH	
maximal baseline B_{max}	0.36	m
HoA at 1 km range distance	52	m

HoA: height of ambiguity; V: vertical polarisation; H: horizontal polarisation.

1.2. Test Sites and Datasets

1.2.1. Davos Strandbad

We first discovered the multipath interferences at the Davos Strandbad test site during a campaign aimed at snow height retrieval. The radar was installed at the Strandbad in Davos (1560 m a.s.l., Grisons, Switzerland) from where the southeast facing Dorfberg mountain slope was monitored. The Dorfberg slope spans a range distance interval of 350 to 2500 m and elevations between 1560 and 2500 m. The campaign took place in the winter seasons of 2015/2016 and 2016/2017. Between December and April, Dorfberg was continuously monitored with 4 min intervals. Dorfberg and Strandbad are separated by a lake called Davosersee, which is drained during the winter months for hydropower production. Between January and April 2016, the lake surface elevation dropped from 1558.3 to 1530.7 m a.s.l. The radar was positioned inside a radar dome (Figure 2a) for weather protection. Figure 2b shows a map of the test site, depicting the regions covered by the radar, the location of the radar, weather stations and corner reflectors.

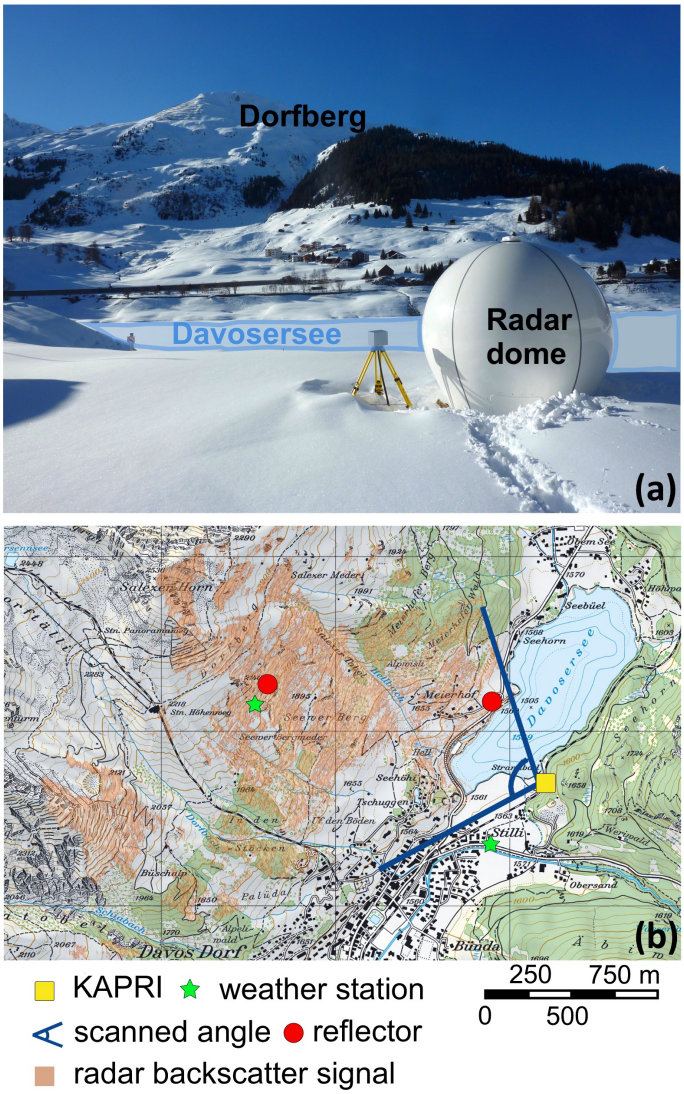

Figure 2. Davos test site. (**a**) the photograph shows the radar (inside a radome for weather protection), the reflective lake (Davosersee) and the observation area (Dorfberg); (**b**) map of the test site showing radar location and coverage, location of reflectors and the weather station.

1.2.2. ETH Hönggerberg

To confirm the findings of the experiment at the Davos Strandbad test site and analyse the influence of the antenna height on multipath interference, we chose a second test site in the vicinity of the ETH Hönggerberg Campus in Zurich, Switzerland, where measurements were performed in a controlled experiment (Figure 3). The test site is a gently ascending slope, gradually steepening from 2° in the near to 4° in the far range. The far range of the image, at range distances beyond 360 m, is a field covered by maize plants with estimated height 1.5 m not visible in Figure 3 . The near range up to a range distance of 200 m was covered with grass of roughly 50 cm in height, which was mowed during the experiment. KAPRI was mounted on a fork lift and measurements were taken at different elevations, from 1 to 6 m of the transmit antennas above ground, with 1 m intervals. During the experiment, the grass was mowed in lines, leaving behind lines of piled up cut grass separated by very short grass.

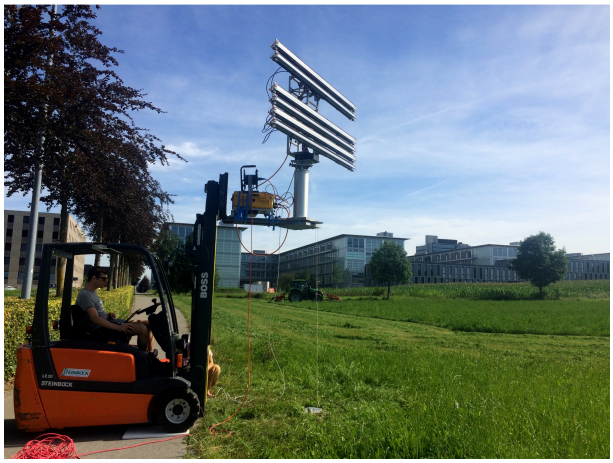

Figure 3. Hönggerberg experiment. The radar is mounted on a forklift to perform measurements at different elevations. In the near range, the lines of short cut grass separated by lines of piled grass and not yet mowed grass is visible. The observation area with a steeper slope is located at the far range and is not visible in the photograph.

2. Model

2.1. Model Description

We designed a model to analyse the behaviour and occurrence of multipath interferences. The model computes the evolution of the amplitude and phase of a point target over time caused by changes of the geometry and simulates the full 2D image for a given geometry. We used the 2 m resolution swissALTI^{3D} Digital Elevation Model (DEM) converted to cylindrical coordinates (azimuth, horizontal distance x and vertical distance y). A sketch of the geometric setup and the modelled raypaths is given in Figure 4.

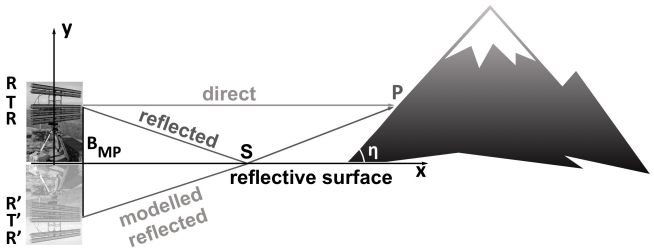

Figure 4. Radar imaging geometry similar to Lloyd's mirror experiment [22]. T and R is the location of the transmit and receive radar antenna, T' and R' the virtual transmit and receive radar antennas, which are the mirror of T and R with the reflective surface. B_{MP} is the multipath baseline that determines the MPI pattern frequency. It is approximately double the distance between the antenna and the reflective surface.

The model is based on raytracing [27]. For each point P along a line with fixed azimuth angle, the travel time of all possible raypaths is computed. For each of the different Transmit (T)–Receive (R) antenna combinations, four different paths along which the waves can travel between the radar and P are possible: The path can be direct TPR, single reflected TPSR/TSPR or double reflected TSPSR. Each letter in this sequence describes a reflection or the transmission/reception of the signal at the antenna. We assume that the reflection takes place on a horizontal surface S between radar and observation area, and we model it as purely specular. We also define the virtual antennas T' and R'.

Their location corresponds to the mirrored location of the real antennas T and R with the surface S. For a horizontal surface and specular reflection, the reflected raypath TSPR has the same length as the direct ray T'PR. The same applies to TPSR and TSPSR, which have the same length as T'PR and T'PR', respectively. Because the direct raypaths from the virtual antennas are easier to model than the real, reflected paths, we implement the virtual paths in the model. The pathlength L is only computed for the DEM points that can be reached by specular reflection on the surface S. Backscatter coefficients are calculated by Equation (1), where $n \in [0,1,2]$ represents the number of reflections on the surface, A the amplitude of the emitted wave and D the polarisation dependent attenuation occurring at each reflection. The phase is determined by raypath length. Each reflection at the surface induces a phase shift of 180° to the wave, which is accounted for by the term -1^n . This condition is imposed by the boundary conditions of the Maxwell equations at the interface between the air and the reflective surface with a higher relative permittivity. By changing the antenna coordinates to match all the possible combinations of the two transmit and four receive antennas of KAPRI, the full MPI affected scattering matrix of an isotropic point target can be simulated. Physical scattering properties are not included in the model, as the generation of the multipath interference pattern is on the first order a purely geometrical phenomenon, if the assumption of a high reflectivity of the surface generating the indirect waves is fulfilled. After computing the distance from the radar to each point in range along the direct, single and double reflected paths, a weighted binning function sums the complex values z_L associated with all travel paths that fall within one range resolution cell (0.75 m). In this way, signals with similar travel times but coming from different regions on the DEM interfere.

$$z_L = (-1)^n \, AD^n e^{i\frac{2\pi L}{\lambda}}. \tag{1}$$

2.2. Theoretical Considerations

The setup described is very similar to Lloyd's mirror experiment [22], which describes the interference of monochromatic light from a direct and an indirect, reflected path. The radar and the virtual radar (Figure 4) act as an additive single pass interferometer with a vertical baseline B_{MP}, hereafter referred to as multipath baseline to distinguish it from the interferometric baseline of the radar itself. As opposed to Lloyd's experiment, our setup is not purely monostatic, as transmit and receive antennas have a vertical spacing of 12–47 cm depending on the antenna combination. This distance is small compared to the range distance to the observation area and thus the bistatic angle is small, enough to approximate our setup as a monostatic setup like in Lloyd's experiment. In such a monostatic case, the multipath baseline is double the distance between the radar antenna and the reflective surface. In reality, in our bistatic case, it is the distance between transmit and receive antenna—where, depending on the considered raypath, either the transmit or the receive antenna location corresponds to the virtual location. From Lloyd's experiment, it was found that, for a given wavelength λ and multipath baseline B_{MP}, the angular spacing in radians of the interference pattern produced by the multipath interference is

$$\theta_f = \frac{2\lambda}{B_{MP}}. \tag{2}$$

From this, we can easily derive the vertical distance d_v between the interference pattern at a range distance R_S

$$d_v \approx R_S \theta = \frac{2R_S\lambda}{B_{MP}}, \tag{3}$$

which leads us to their spacing or local wavelength λ_{MPI} , when projected onto a slope with slope angle η

$$\lambda_{MPI} = \frac{2R_S\lambda}{B_{MP}\sin\eta}. \tag{4}$$

With this simple approximation it is possible to roughly verify the model output. From Equation (4), it can be seen that the MPI pattern spacing is inversly proportional to the multipath baseline.

2.3. Application of the Model

To simulate the spatial pattern and the temporal evolution of multipath interferences in the Davos and Hönggerberg test sites, we implemented the model for both test sites with their respective variables, i.e., the changing surface elevation of Davosersee and KAPRI antenna elevation over ground in the Hönggerberg test site. The aim of this was to analyse the evolution of the multipath interference pattern with changes of the vertical distance between the radar antennas to the reflecting surface, the spatial distribution of the pattern for a given situation and to compare these findings to the measured data. Changes in the vertical distance between radar and surface were achieved either by lowering the reflection surface—by draining the lake in Davos—or by increasing the antenna height—by raising KAPRI higher above the ground in the Hönggerberg test site. The main input parameter is in both cases the 2 m resolution swissALTI^{3D} DEM in cylindrical coordinates resampled to 10 cm resolution. For Davos, the lake surface level given by the DEM was replaced by values provided by Repower (Poschiavo, Switzerland), the company in charge of the lake drainage, with a 10 min temporal resolution. The Davos DEM is thus dependent on time. For the Hönggerberg test site, the DEM is constant, but the antenna elevation over the ground is varied to simulate the different measurements of thef Hönggerberg experiment, whereas, in Davos, the assumption of a horizontal reflection surface—the lake—holds, assuming no turbulence on the lake, such as waves, in the Hönggerberg test site, the near-range area where the reflection occurs is inclined by 2°. The surface was approximated to be horizontal in order to enable the application of the model without further modifications. We chose the maximal height of the surface as height for the entire approximated region to avoid a step at the border to the observation area. This approximation leads to a deviation to the true DEM of a few meters and to slightly different raypath lengths. However, the spatial frequency change relative to the KAPRI antenna height is preserved and thus the approximation is justified in the context of this study.

For the Hönggerberg test site, a simulated full 2D image is computed for the different heights of KAPRI above the ground. These simulated results, especially shape and frequency change of the MPI pattern, are directly relatable to the results of the experiment. To generate the 2D image, the model is run along each azimuth line of the DEM.

Also for the Davos test site, a full 2D image for a given time with its corresponding lake level is computed. Additionally, the model is executed along one azimuth line for different multipath baseline values, i.e., different lake elevation levels. For each value of B_{MP}, the pixel value of a point target is extracted, resulting in the temporal evolution of the radar response of the target. This temporal evolution can be compared to the measured temporal signal on a corner reflector at that location.

The model does not consider specific surface scattering properties. Therefore, the modelled intensity is only a function of the local slope and the DEM resolution. This dependency comes from the fact that the travel time is computed for each DEM point and subsequently binned into 0.75 m range distance bins, corresponding to the range resolution of KAPRI. The finer the DEM resolution and the steeper the slope, the more values are added into one range cell. Therefore the modelled intensity is only a relative measure. Furthermore, polarimetric and interferometric phase values are only a function of the topography and the location of the different antennas. Speckle can be included into the model by randomizing the scattering coefficients of the observed area. To make the MPI pattern visible, multilooking needs to be performed, by averaging over several model iterations with random amplitudes. After 100 iterations, the results from the model including speckle and the model using constant amplitude for each raypath converge. To reduce the computation time, all model results are generated using a constant amplitude.

Because only specular reflection is considered in the model, only areas that can be reached through specular reflection exhibit MPI patterns. In reality, however, the reflection may not be purely specular and the surface not perfectly horizontal, such that even larger areas can be affected. It is therefore expected that the extent of the modelled MPI pattern is smaller than the one of the measured pattern.

3. Results: Measured and Modelled Multipath Interferences

In this section, we discuss measured multipath interferences from the Davos and Hönggerberg test sites and compare them to the model results.

3.1. Influence of Polarisation and Slope Angle

To analyse how well the model can reproduce the multipath interference pattern, we compare the simulated backscatter intensity images to the measured data with different polarisations. It is important to note that, because the MPI signal falsifies the signal at the corner reflectors and thus the measured radar cross section of the reflector, it is not possible to perform radiometric calibration. Therefore, the measured intensity is only a relative quantity, just like the modelled intensity. Figure 5 shows the occurrence of MPI pattern in the Davos test site on the 31 December 2015 in measured backscatter intensity images from horizontally and vertically polarised waves (HH—horizontal transmit and receive, VV—vertical transmit and receive) and a comparison to the model corresponding to the lake surface elevation at that time. Two representative regions A1 and A2 are analysed to illustrate the findings. In region A1, which is a gently sloping meadow, the MPI signal is well visible in both polarisation channels and the model. The MPI pattern frequency and shape are very similar in all three scenarios. In region A2, a higher frequency MPI pattern is visible in HH, which are weaker in VV and invisible in the model. The higher frequency is due to a steeper local slope. The difference between the HH and VV channel suggests that the reflection on the reflection surface is polarisation dependent and stronger in HH than in VV. Region A2 is not illuminated by waves reflected purely specularly on the lake surface; therefore, no interference pattern is visible in the model in this region.

For a more quantitative assessment of the model accuracy, Figure 6 shows a comparison between the measured and modelled backscatter intensity signal along azimuth line 1750 shown as the white line L1 in Figure 5. The model correctly simulates the MPI pattern frequency. To reduce speckle, the signal of 10 neighbouring azimuth lines was averaged. For the sake of consistency, this was done for the measured and modelled dataset, even though the model does not have speckle. As polarisation of the waves and scattering properties are not implemented in the model, we only show the modelled data from the VV antenna pair, which differs from the HH pair only by a slightly different antenna location. Yellow dots represent the modelled intensity, black crosses the measured VV and turqoise plus signs the measured HH intensity from the December dataset. For easier comparison, the model intensity was scaled to match the order of magnitude of the measured intensity. Additionally, as already seen qualitatively in Figure 5, the amplitude of the MPI in the HH channel is roughly by a factor of 10 larger than in the VV channel.

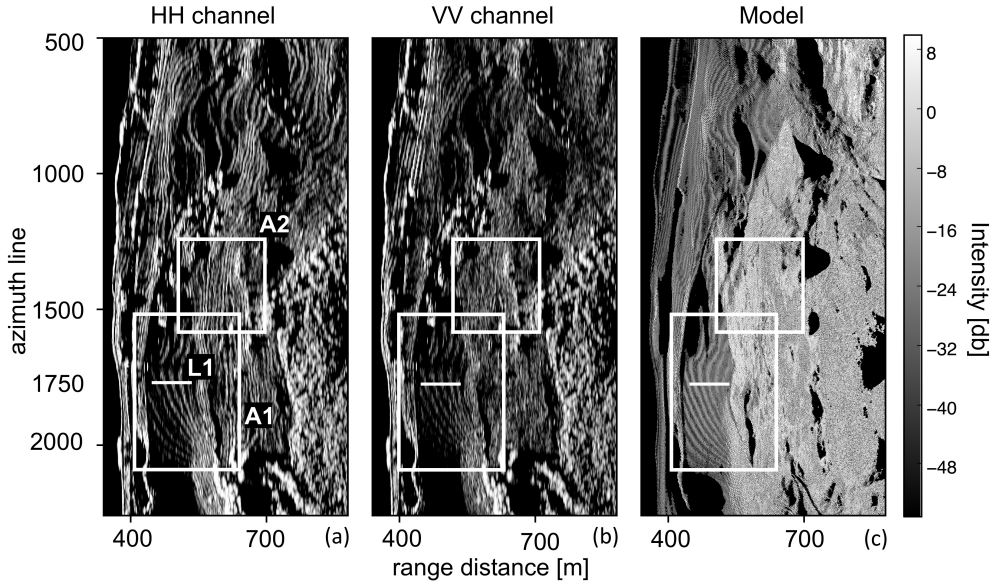

Figure 5. Radar backscatter images showing an MPI pattern at the Dorfberg test site in (**a**) horizontal and (**b**) vertical polarisation compared with (**c**) the modelled MPI. Area A1 highlights an area with a strong, low frequency MPI signal that are well visible in both polarisations and the model. Area A2 shows a higher frequency signal due to a steeper slope that are visible in the backscatter intensity image of the horizontal wave polarisation but hard to discern in the vertical polarisation and not present in the model. The white line corresponds to the central azimuth line used for the computation shown in Figure 6.

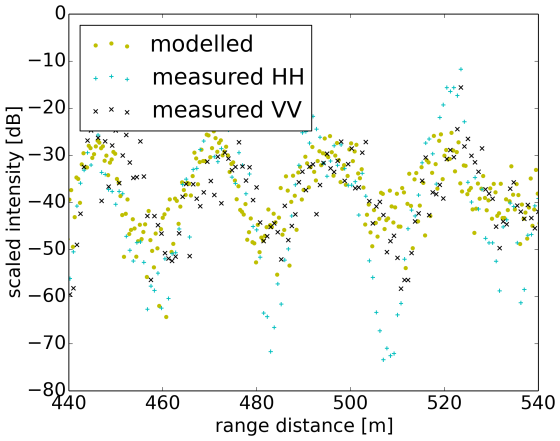

Figure 6. Measured HH and VV and modelled backscatter intensity averaged along 10 neighbouring azimuth lines. The modelled intensity is scaled to match the order of magnitude of the measured intensity.

3.2. Influence of the Reflection Surface Scattering Properties

The reflection properties of the reflective surface play a crucial role in the occurrence of the MPI. This was already suggested by the difference in the MPI signal intensity between the different polarisations in Figure 5. If the surface between radar and observation area is highly reflective, strong multipath interferences are expected to be generated. If, on the other hand, the surface exhibits volume or non-directional surface scattering, the interference pattern should be weaker due to less energy reaching the observation area through the indirect path. To show this, we compare two backscatter intensity images from the Hönggerberg test site with different surface properties. In Figure 7a,

the reflecting surface is covered by high grass, which causes nonspecular volume scattering, whereas, in Figure 7b, the grass has been cut and bare soil/short grass is exposed between lines where the cut grass is deposited. Bare soil or very short grass produce specular reflections. The different reflection properties between these lines result in dark and bright lines in the near range, which must not be confused with the MPI pattern in the observation area surrounded by a white polygon. In Figure 7a, the MPI signal in the observation area is much weaker than in Figure 7b, which corresponds to the transition from volume to specular surface reflection on the reflective surface. This experiment shows the crucial role of scattering properties of the reflecting surface. In the Davos test site, this effect is very visible as well. Freezing of the lake and snowfall covering the frozen lake both reduce the specular nature of the reflection and thus reduce the strength of the MPI. Wetting of the snow surface, on the other hand, increases the reflectivity and thus also increases the MPI.

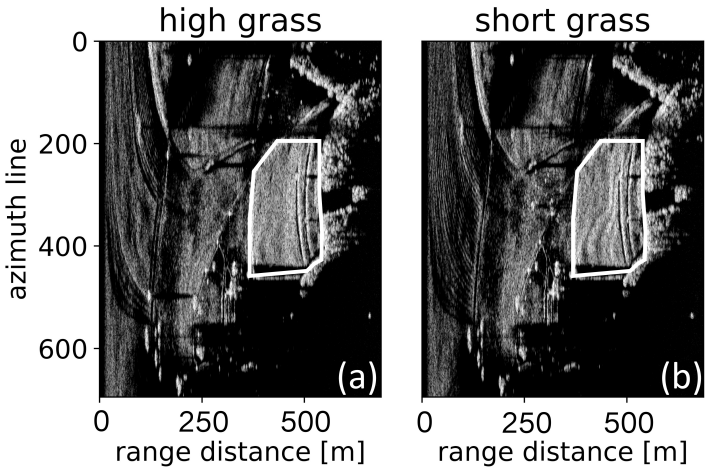

Figure 7. Measured MPI in the Hönggerberg test site with varying scattering properties. (**a**) high grass prevails in the near range (range distance less than 200 m) and only a small area has been mowed, while, in (**b**), the entire field in the near range has been mowed and the remaining short grass results in strong specular reflection. In the observation area (range distance 400–500 m), the MPI signal is much stronger when very short grass is exposed.

3.3. Influence of Changing Multipath Baseline

3.3.1. First Order Effects Visible in the Backscatter Intensity Data

According to Equation (4), the MPI pattern frequency is proportional to the multipath baseline. To demonstrate this proportionality, we performed an experiment at the Hönggerberg test site, where data was acquired at different antenna elevations. Figure 8 shows the measured and modelled backscatter intensity images for the different antenna elevations. The upper row shows the results for an elevation of 1 m above the ground of the lowest antenna, the lower row for 2 m elevation. Both the measurement (on the left) and model (on the right) show a clear increase, corresponding to roughly a doubling in the MPI pattern frequency with a doubling of the multipath baseline. Thus, in the backscatter intensity data, a change in the multipath baseline manifests simply as a visible change in the MPI pattern frequency.

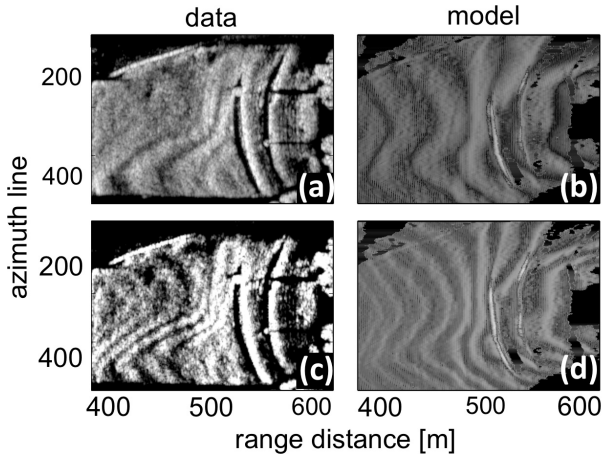

Figure 8. Measured and modelled MPI in the Hönggerberg test site with different antenna elevations. The upper rows (**a**,**b**) were measured and modelled with an antenna elevation of 1 m, while the lower rows (**c**,**d**) correspond to an antenna height of 2 m.

3.3.2. Second Order Effects Visible in the Interferometric and Polarimetric Data

The effect is less straightforward in the polarimetric and interferometric data. To analyse it, we looked at the Davos test site data, where the lake surface elevation dropped continuously over the course of the measurement campaign. With the lake surface acting as the main reflective surface, this corresponds to a steady increase in the multipath baseline causing in increase in the MPI pattern frequency. In comparison to the Hönggerberg experiment where we performed measurements at different heights in 1 m intervals, here we have measurements every 4 min, corresponding to small lake level changes of less than 1 mm. This allows to not only see the difference between two discrete values, but to track the gradual changes in the multipath interference signal and observe a slow frequency change of the MPI pattern as the multipath baseline changes. Because the transmit and receive antennas of the horizontal and vertical polarisation are located at different elevations, the path length change associated with the lake level drop is different for the two antenna pairs. Therefore, the MPI signal evolves slightly differently over time for each antenna pair, resulting in a second order interference pattern that appears when combining the data from the two antenna pairs. The same applies to single pass interferometric data. In a scenario unaffected by multipath interferences, the copolar phase is zero on a corner reflector or has a constant phase offset in the case of an uncalibrated system, and the interferometric phase also has a stable value on the corner reflector. Figure 9 shows the copolar phase over time measured on a corner reflector located in an area affected by MPI and the modelled phase for this resolution cell. The copolar phase is not stable and varies in a periodic manner over the entire 2π phase space. For better visibility of the cycles, the data was only plotted over a seven-day time window. A comparison of the measured and modelled phases shows that the model can reproduce well the frequency of this second order interference pattern, whereas the amplitude and shape of the phase variations is not always well reproduced. We found that several parameters have a strong influence on shape and amplitude of the variations: the polarisation dependent reflection coefficient as well as the phase offset between the two polarisations in the case of our uncalibrated system. Due to the presence of MPI, it was impossible to phase calibrate KAPRI and thus all of these parameters are unknown. A change in the polarisation dependent reflection coefficients reproduced the change from smaller to bigger amplitude variations on 12 January. Heavy snowfall occurred on that day for the first time in the season and was probably at the origin of these changes. It is important to note that, even though this second order interference pattern is demonstrated here in the polarimetric data, it is not a real polarimetric effect and is solely based on the geometric arrangement of the antennas, which makes the polarimetric measurements vulnerable to MPI.

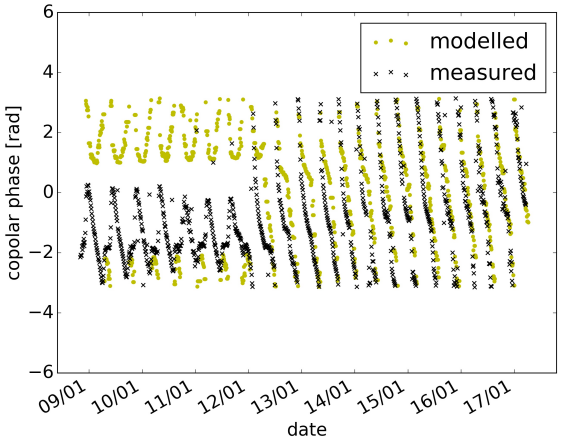

Figure 9. Time series of modelled and measured copolar phase variations induced by changes of the Davosersee lake surface level on a corner reflector.

3.3.3. Fourth Order Effects Visible in the Difference of Single Pass Interferograms

A similar problem arises when combining acquisitions separated temporally, if the reflective surface changes over time, such as was the case in the Davos test site. Over the course of the season, due to a reduction in the specular nature of the reflection, the MPI signal became almost indiscernible in the backscatter data, suggesting that multipath interference becomes negligible. However, especially at small interferometric baselines (here $B = 36$ cm), even the smallest phase errors in interferograms can lead to large errors in a DEM. We observed this in the difference of two single pass interferograms, separated by a timespan during which the lake surface dropped, but no other major changes occurred in the scene. Due to the change in lake level, the interference pattern in both interferograms is slightly shifted in space and frequency. In the interferogram difference, the interference pattern does therefore not cancel out and will instead exhibit clear phase undulations. An example for such phase undulations is shown in Figure 10, which is the difference of 10 averaged consecutive interferograms from midnight of 17 March and 18 March 2016 with corresponding lake surface elevations of 1538.2 and 1537.8. With a baseline of 36 cm, these phase variations correspond to deviations of several meters. On these dates, the MPI pattern was not easily visible in the intensity images. Nevertheless the undulations in the interferogram difference show that weak multipath interference can deteriorate or bias the data even if not visible at first sight in intensity images or single pass interferograms.

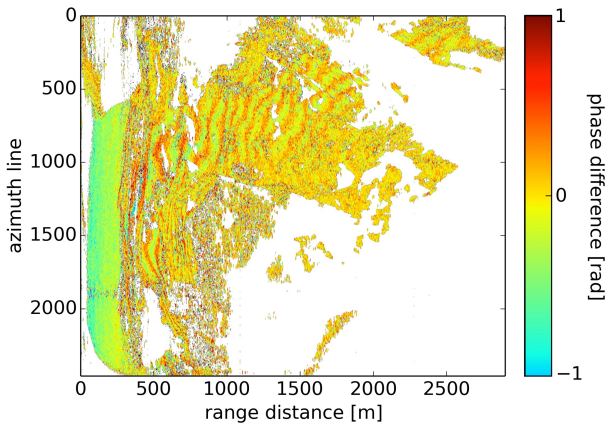

Figure 10. Differences between two single pass interferograms separated by a temporal baseline of 24 h associated with a lake surface drop of 0.4 m. Each of the two interferograms was computed as an average over 10 consecutive interferograms in a timespan of 40 min.

4. Discussion

4.1. Occurence of MPI in Satellite- and Ground-Based Radar Data

Both our model and the two different experiments at Davos Dorfberg and ETH Hönggerberg show that the observed pattern originates from multipath interferences. Both test sites had a similar upward looking geometry, but different incidence angles and scattering properties. Careful investigation of the phenomenon showed that three different conditions need to be met for MPI to occur. Figure 11 summarizes them and illustrates the geometric restrictions. The first condition (C1), which can not be visualised in Figure 11, is the presence of a reflective surface, where a part of the antenna-beam is reflected and reaches the observation area over an indirect path. This implicitly requires a beamwidth that illuminates both the reflective surface and the observation area. In a first step, it is assumed that the reflective surface is horizontal. The geometrical conditions are later extended to the non-horizontal case. The incidence angle θ is defined as the angle between slant range and the vertical.

For interference to occur, the reflected wave needs to illuminate the area that is also reached by the direct wave (condition C2, Figure 11a,b). The average slope angle is defined as the $\eta = \arctan \frac{H}{d}$, where H is the height of the mountain above the reflection surface and d the horizontal length of the slope. For the reflected wave to be intercepted by the mountain, it is necessary that $D \tan(90^\circ - \theta) < d \tan \eta$, with D being the horizontal distance between the reflection point and the mountain summit. From this inequality, we can extract a simple condition as a rule of thumb that multipath interference occurs if $\eta > 90^\circ - \theta$. With such a rule of thumb, involving only the slope and incidence angles, it is possible to broadly estimate in which geometries MPI is likely to occur.

However, when planning a specific campaign where MPI cannot easily be ruled out, it is recommended to use the full inequality, to check whether MPI may occur. For non-horizontal reflective surfaces, condition C2 becomes more complex and involves the slope angle γ of the reflection surface. The reflection illuminates the mountain if C2' $d \tan \eta > h + (D - d) \tan(90^\circ - (\theta + 2\gamma))$ is fulfilled, where h is the height of the reflection (Figure 11c,d). With the same argument as for C2, we extract the rule of thumb that $\eta > 90^\circ - (\theta + 2\gamma)$ needs to be fulfilled for MPI to occur.

MPI patterns are only visible if the slope is not in radar layover, i.e., the incidence angle θ needs to be larger than the slope angle η (condition C3, Figure 11e,f). By combining the geometrical constraints (conditions C2 and C3, Figure 11g), only a small region corresponding to the triangle surrounded by a thick black line in (g) and defined by defined by $|\eta - 45^\circ| \leq \theta - 45^\circ$ fulfills all geometrical conditions, which allows for the occurrence of MPI. For satellite-borne radar data, these conditions are very unlikely to be fulfilled, especially in combination with condition C1. Indeed, incidence angles above 45 degrees in combination with a restricted repertoire of slope angles are required. Satellites generally acquire at incidence angles below 60°, e.g., 29–46° (Sentinel) or 20–55° (TerraSAR-X). The minimal required slope angle η is given by $90^\circ - \theta$ and hence, at incidence angles of up to 55°, slope angles steeper than 35° are necessary. In the medium incidence angles of about 45° , very steep slopes of 45° are needed. Therefore, for horizontal reflection surfaces, the occurrence of MPI can be almost excluded for satellite data. As seen in Figure 11g, C2' is more likely to be fulfilled than the original condition C2, such that slopes with slope angles of less that 45° could also be affected. However, for well developed MPI patterns, the reflective surface needs to be relatively homogenous and reflective, which is rarely the case for inclined surfaces. It is therefore possible that, in such cases, MPI occurs but cannot easily be detected.

For upward looking ground-based radar, much larger incidence angles of almost 90° onto the horizontal reflection surface are achieved, such that condition C2 is fulfilled for almost any mountain slope. For such systems, the incidence angle onto the mountain slope is also high enough to fulfill condition C3 in most cases. It is important to note that, for ground-based radars, the incidence angle over the monitored region can vary considerably and thus care needs to be taken when applying the established conditions.

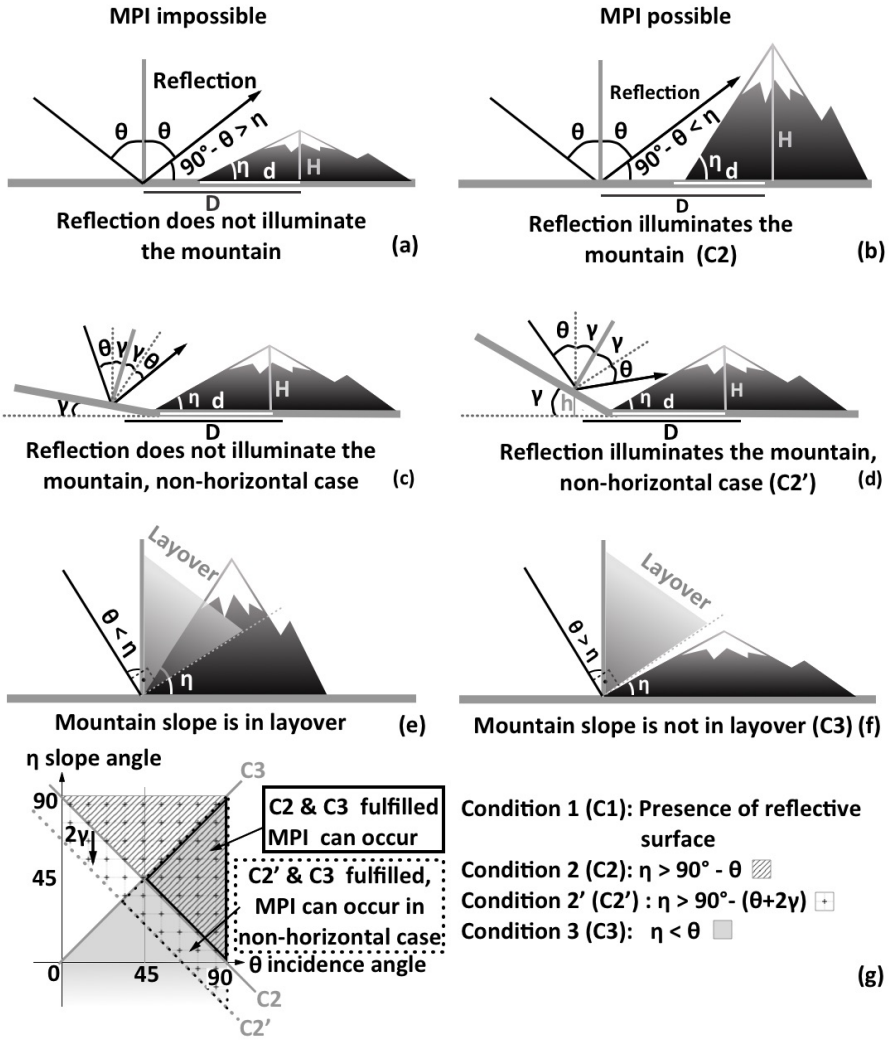

Figure 11. Conditions for the occurrence of MPI. (**a**–**f**) illustrate the geometrical requirements for the occurrence of multipath interference; (**g**) gives a visual and text summary of all geometrical and non-geometrical conditions.

From the above considerations, it can be concluded that MPI is unlikely to occur in satellite based radar images. However, in ground-based upward looking systems, the geometrical conditions are often met and the presence of a reflective surface in the near range of the radar will result in MPI, which deteriorates the data. Even though in this study we used KAPRI, our real aperture radar with interferometric and polarimetric capabilities, it is important to note that the MPI problematic is not limited to KAPRI or systems with similar antenna arrangements and interferometric or polarimetric capabilities. Any ground-based radar, synthetic or real aperture, with a large elevation aperture can be affected. These large elevation beamwidths are often necessary to enable monitoring of large areas, if the radar has no beam-steering capabilities. MPI may also appear in airborne data acquired with a large beamwidth at large incidence angles in mountainous terrain adjacent to a reflective surfaces such as lakes. In ground-based and in airborne setups, one must take care of all objects and surfaces surrounding the antennas, such as, for example, wings of the plane or walls to which the antennas are fixed.

4.2. Avoiding MPI

The best way to avoid MPI is to chose a measurement geometry that is not prone to multipath interferences. For ground-based radar campaigns, it is advised to install the radar in an elevated area, such that the geometrical conditions for multipath interference (Figure 11) are not met or such that the beamwidth is not wide enough to hit both the reflective surface and the observation area. In alpine regions, it is often possible to position the radar on the slope of the valley side opposing the observation area. However, this implies a large range distance to the target, which, in the case of real aperture systems such as KAPRI, results in coarse azimuth resolution and large heights of ambiguity. If only a small area is to be observed, it is advisable to use antennas with a narrow elevation beamwidth to avoid multipath interferences. If geometrical prevention of MPI is not possible, shielding of the reflective surface is required. This was done in the Davos test site—the construction of a 1.6 m high wall, inclined in a 60° angle at a distance of 3 m around the radar rotation axis, avoiding the illumination of the reflecting lake. The wall was a timber scaffolding, covered with an aluminium net with mesh size of 6 mm, which is less than half the wavelength (1.7 cm). Figure 12a shows the radar dome with the shielding wall under construction. Due to the inclination angle, all waves hitting the construction are deflected to the sky, whereas the remaining part of the antenna beam reaches the target slope undisturbed. The construction led to an almost complete suppression of the MPI signal for the lower antennas, as seen in Figure 12b–d, displaying the backscatter intensity of measurements performed with and without shielding, respectively. In Figure 12d, it is clear that even though the MPI signal is strongly reduced, a slight perturbation of the measured signal remains. The overall intensity is reduced due to partial shadowing of the wave-beam reaching the area. The remaining perturbation can probably be explained by diffraction on the edges of the shield, which probably results in some waves reaching the reflective surface despite the shielding. Additionally due to the vertical alignment of the six antennas, in total separated by 85 cm, it is impossible to shield all antennas equally well without losing a considerable part of the observation area signal for the lower antennas. Therefore, the upper antennas are still mildly affected by multipath inference, which makes the retrieval of accurate single pass interferograms impossible.

The Hönggerberg experiment showed that, by increasing the elevation of the antennas above the reflective surface, the MPI pattern frequency is strongly increased. Due to limitations of the measurement setup, it was not possible to increase the antenna elevation to more than 6 m above the reflective surface. However, with a further increase, it may be possible to decrease the wavelength of the MPI pattern to length scales below the order of magnitude of the resolution cell size. This would make them invisible, but the accuracy of the data is not necessarily restored, as the pixel value is still influenced by the indirect ray path.

The importance of the scattering properties of the reflective surface has been demonstrated in Figure 7. The higher the reflectivity of the surface, the stronger the MPI pattern will appear. This suggests that if an upward looking geometry prone to MPI is adopted, it is favourable to have a surface that exhibits random rather than specular oriented scattering. The following non-exhaustive list of surfaces should be avoided: water, wet snow, bare soil, short grass, and tarred areas.

Detecting MPI in the data may not always be an easy task. When the interference is very strong, they are easily detected in the backscatter intensity images. Which of the observables is easiest to detect them depends on the nature of the reflecting surface and the antenna configuration of the radar. For a changing surface, such as the lake in the Davos test site, differencing of single pass interferograms acquired at different times, or a timeseries of a stable target, are good indicators. However, if the reflecting surface doesn't change in elevation or in scattering properties, e.g., a tarred area, no changes will be visible. Due to the different multipath interference pattern superimposed to the direct radar signal for different antenna locations, the interferometric coherence shows low values in the MPI pattern and is therefore a good indicator for MPI if no changing reflective surface is present.

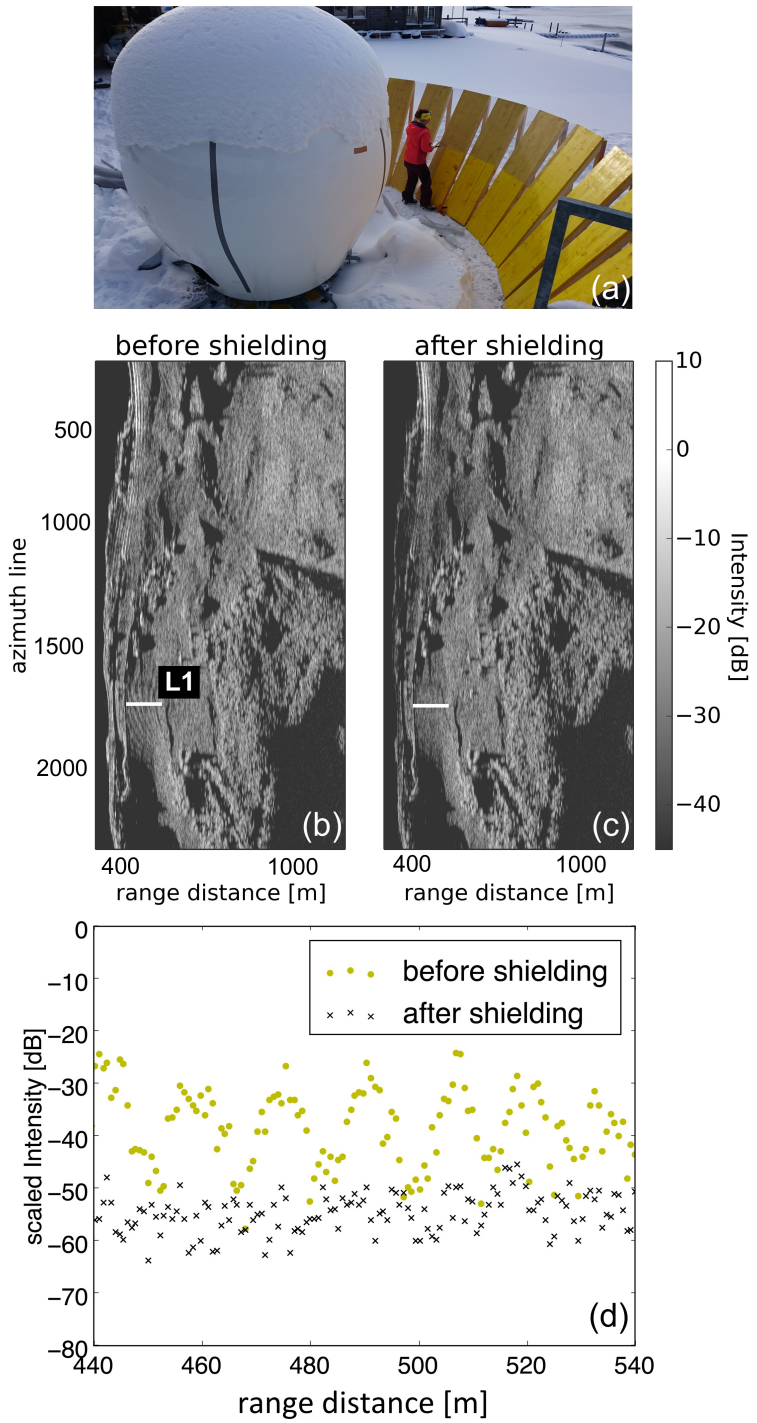

Figure 12. (**a**) photo of the shielding setup. The wooden scaffolding is covered with a fine-meshed (6 mm) aluminium grid; (**b**) backscatter intensity images before and (**c**) after shielding of the reflective surface. The MPI pattern is strongly reduced; (**d**) backscatter intensity along L1 averaged over 10 neighbouring azimuth lines before and after shielding; (**a**–**d**) illustrate the geometrical requirements for the occurrence of multipath interference.

4.3. Limitations of the Model

With the developed model, it has been possible to satisfactorily reproduce occurrence, location and frequency of the MPI pattern, in order to pinpoint their origin and the most important parameters influencing them, i.e., multipath baseline, reflection surface properties and geometry of the setup. However, as the angular dependent bidirectional scattering function of the reflective and the observation surface are not known, the model cannot simulate the measured complex scattering coefficients, even though it correctly reproduces location and frequency of the MPI pattern. Therefore, the model cannot be used to correct MPI affected data. Additionally, only purely specular reflection on a horizontal surface is considered, limiting the geometric distribution of the MPI pattern to a smaller area than in reality, where a wider range of incidence angles of the reflected wave onto the slope are possible.

To achieve a better accuracy of the full MPI pattern distribution, it would be necessary to implement reflections on non-horizontal surfaces and allow for non-specular reflections on that surface. The current model was designed using the fact that the reflected raypath TSPR has the same length as the direct ray T'PR emitted from a virtual wave source (Figure 4). This is only true for specular reflections on horizontal surfaces. To include non-specular reflections, a new implementation is required to model the real travel path of the indirect rays. Such an advanced model including both, non-specular reflections and non-horizontal reflective surfaces would allow for any potential radar location to be tested for the occurrence of MPI, which would be a useful tool for anyone designing a ground-based radar campaign. In the current study, we aimed to understand the origin of the MPI pattern and its behaviour to changes of different parameters. Still, the model successfully reproduced the frequency and location of the MPI pattern even for a slightly inclined surface, which we approximated as horizontal. An advanced model covering all possible topographies is out of the scope of this study, but our model already covers the most common geometry.

5. Conclusions

We showed that multipath interferences in radar images can be caused by the superposition of direct waves and indirect waves that have been reflected at a surface between radar and observation area. The resulting interference pattern appear in all orders of statistical signal evaluation: in intensity images, coherence and phase of all interferometric and polarimetric covariances and also in interferometry derived DEM differences. We found that they have negligible effect on repeat-pass differential interferograms with short temporal baselines compared to the timescale on which the reflective surface changes. In the case of an invariant reflective surface, differential interferometry and DEM differences are unaffected by MPI. In the affected areas, an absolute calibration of the intensity and polarimetric phase with corner reflectors is impossible, as the return from the reflectors is biased by the indirect wave, which superimposes the direct signal. In the case of a changing reflective surface, also relative calibration over time is impossible, as the contribution of the superimposed wave changes with time. This was observed at the Davos test site, where the lake surface elevation changed over time. Davos was a special case with the draining lake as reflecting surface; however, many different types of surfaces can be subject to slight changes in the reflection properties, e.g., vegetation height, which could result in a temporally variable interference pattern.

We found that MPI can occur in ground-based radar measurements with an upward looking geometry but are unlikely in satellite radar data. Especially affected are scenarios, where the observation areas and the radar are separated by a highly reflective flat surface, such as water, bare soil, short grass or wet snow. However, we want to stress that it may still be possible to acquire meaningful data under such conditions. We have observed MPI in our two test sites and could prove the origin of the pattern using our model, but considering that ground-based systems have been operational for years and the phenomenon has not been reported so far, we expect that, in many ground-based field studies, MPI does not occur or is not well pronounced.

The appearance of MPI signal in the radar image significantly deteriorates the data and makes retrieval of most physical parameters impossible. To avoid MPI, it is recommended to place ground-based radars in elevated areas, to allow for a downward looking geometry, where the antenna pattern is such that the reflected radiation cannot illuminate the observation area. Another possibility is the shielding of the reflective surface, such that only the observation area is illuminated by the radar waves. However, a proper shielding for all antennas can be difficult depending on the antenna arrangement and the diffraction of the microwaves.

To predict the occurrence of MPI, we developed a model that can simulate the MPI in the geometry of the two test sites. The simulation reproduces the MPI successfully; however, a more detailed modeling approach would be needed to implement non-specular reflections and reflections on non-horizontal surfaces. With such a model, the possible—geometrically induced—occurrence of MPI could be predicted for most prospective test sites.

The additive superposition of multiple radar waves with different travel paths causing MPI is very similar to the method used to retrieve the first DEMs from additive superposition of the complex radar images acquired with spatially separated antennas [28]. Thus, if the exact position of the reflection is known, it would be possible to extract the topography from the MPI pattern as described in [28]. However, modern interferograms computed by multiplicative correlation are much more precise and easier to interpret after phase unwrapping [29]. Therefore, the practical use of the MPI is by far outweighed by their destructive nature of the direct signal and they should be avoided whenever possible by choosing a proper imaging geometry.

Acknowledgments: This work has been funded by the Swiss National Fund under the contract number 200021 156014. The Davosersee surface elevation data was crucial for the development of the model and we would like to thank Repower for providing the data.

Author Contributions: All authors conceived the study. Célia Lucas, Silvan Leinss and Yves Bühler performed the experiments. Célia Lucas analyzed the data with support from Armando Marino and Silvan Leinss. Célia Lucas wrote the manuscript, which was thoroughly revised and edited by Silvan Leinss, Armando Marino, Yves Bühler and Irena Hajnsek.

Conflicts of Interest: The authors declare no conflict of interest.

References

1. Antonello, G.; Casagli, N.; Farina, P.; Leva, D.; Nico, G.; Sieber, A.J.; Tarchi, D. Ground-based SAR interferometry for monitoring mass movements. *Landslides* **2004**, *1*, 21–28.
2. Calabro, M.D.; Schmidt, D.A.; Roering, J.J. An examination of seasonal deformation at the Portuguese Bend landslide, Southern California, using radar interferometry. *J. Geophys. Res.* **2010**, *115*, 1–10.
3. Casagli, N.; Catani, F.; Del Ventisette, C.; Luzi, G. Monitoring, prediction, and early warning using ground-based radar interferometry. *Landslides* **2010**, *7*, 291–301.
4. Leva, D.; Nico, G.; Tarchi, D.; Fortuny-Guasch, J. Temporal analysis of a landslide by means of a ground-based SAR interferometer. *IEEE Trans. Geosci. Remote Sens.* **2003**, *41*, 745–752.
5. Mazzanti, P.; Brunetti, A. Assessing rockfall susceptibility by Terrestrial SAR Interferometry. In Proceedings of the Mountain Risks International Conference, Firenze, Italy, 24–26 November 2010; pp. 109–114.
6. Pieraccini, M.; Casagli, N.; Luzi, G.; Tarchi, D.; Mecatti, D.; Noferini, L.; Atzeni, C. Landslide monitoring by ground-based radar interferometry: A field test in Valdarno (Italy). *Int. J. Remote Sens.* **2003**, *24*, 1385–1391.
7. Tarchi, D. Monitoring landslide displacements by using ground-based synthetic aperture radar interferometry: Application to the Ruinon landslide in the Italian Alps. *J. Geophys. Res.* **2003**, *108*, 2387.
8. Tarchi, D.; Antonello, G.; Casagli, N.; Farina, P.; Fortuny-Guasch, J.; Guerri, L.; Leva, D. On the use of ground-based SAR interferometry for slope failure early warning: The Cortenova Rock Slide (Italy). In *Landslides: Risk Analysis and Sustainable Disaster Management*; Springer: Berlin/Heidelberg, Germany, 2005; pp. 337–342.
9. Del Ventisette, C.; Intrieri, E.; Luzi, G.; Casagli, N.; Fanti, R.; Leva, D. Using ground based radar interferometry during emergency: The case of the A3 motorway (Calabria Region, Italy) threatened by a landslide. *Nat. Hazards Earth Syst. Sci.* **2011**, *11*, 2483–2495.

10. Rödelsperger, S.; Läufer, G.; Gerstenecker, C.; Becker, M. Monitoring of displacements with ground-based microwave interferometry: IBIS-S and IBIS-L. *J. Appl. Geodesy* **2010**, *4*, 41–54.
11. Severin, J.; Eberhardt, E.; Leoni, L.; Fortin, S. Use of Ground-Based Synthetic Aperture Radar to Investigate Complex 3-D Pit Slope Kinematics. In Proceedings of the Slope Stability 2011: International Symposium on Rock Slope Stability in Open Pit Mining and Civil Engineering, Vancouver, BC, Canada, 18–21 September 2011; pp. 1991–1996.
12. Luzi, G.; Pieraccini, M.; Mecatti, D.; Noferini, L.; Macaluso, G.; Tamburini, A.; Atzeni, C. Monitoring of an alpine glacier by means of ground-based SAR interferometry. *IEEE Geosci. Remote Sens. Lett.* **2007**, *4*, 495–499.
13. Riesen, P.; Strozzi, T.; Bauder, A.; Wiesmann, A.; Funk, M. Short-term surface ice motion variations measured with a ground-based portable real aperture radar Interferometer. *J. Glaciol.* **2011**, *57*, 53–60.
14. Leinss, S.; Wiesmann, A.; Lemmetyinen, J.; Hajnsek, I. Snow Water Equivalent of Dry Snow Measured by Differential Interferometry. *IEEE J. Sel. Top. Appl. Earth Obs. Remote Sens.* **2015**, *8*, 3773–3790.
15. Caduff, R.; Wiesmann, A.; Bühler, Y.; Pielmeier, C. Continuous monitoring of snowpack displacement at high spatial and temporal resolution with terrestrial radar interferometry. *Geophys. Res. Lett.* **2015**, *42*, 813–820.
16. Caduff, R.; Wiesmann, A.; Bühler, Y.; Bieler, C.; Limpach, P. Terrestrial radar interferometry for snow glide activity monitoring and its potential as precursor of wet snow. In Proceedings of the 13th Congress Interpraevent, Lucerne, Switzerland, 30 May–2 June 2016; pp. 239–248.
17. Martinez-Vazquez, A.; Fortuny-Guasch, J. A GB-SAR processor for snow avalanche identification. *IEEE Trans. Geosci. Remote Sens.* **2008**, *46*, 3948–3956.
18. Noferini, L.; Pieraccini, M.; Mecatti, D.; Macaluso, G.; Luzi, G.; Atzeni, C. DEM by ground-based SAR interferometry. *IEEE Geosci. Remote Sens. Lett.* **2007**, *4*, 659–663.
19. Strozzi, T.; Werner, C.; Wiesmann, A.; Wegmuller, U. Topography mapping with a portable real-aperture radar interferometer. *IEEE Geosci. Remote Sens. Lett.* **2012**, *9*, 277–281.
20. Caduff, R.; Schlunegger, F.; Kos, A.; Wiesmann, A. A review of terrestrial radar interferometry for measuring surface change in the geosciences. *Earth Surf. Process. Landf.* **2015**, *40*, 208–228.
21. Monserrat, O.; Crosetto, M.; Luzi, G. A review of ground-based SAR interferometry for deformation measurement. *ISPRS J. Photogramm. Remote Sens.* **2014**, *93*, 40–48.
22. Lloyd, H. On a New Case of Interference of the Rays of Light. *Trans. R. Ir. Acad.* **1831**, *17*, 171–177.
23. Bolton, J. Radio astronomy at Dover Heights. *Proc. Astron. Soc. Aust.* **1982**, *4*, 349–358.
24. Mrstik, A.; Smith, P. Multipath limitations on low-angle radar tracking. *IEEE Trans. Aerosp. Electron. Syst.* **1978**, *14*, 85–102.
25. Werner, C.; Andreas, W.; Strozzi, T.; Kos, A.; Caduff, R.; Wegmuller, U. The GPRI Multi-mode Differential Interferometric Radar for Ground-based Observations. In Proceedings of the 9th European Conference on Synthetic Aperture Radar, Nuremberg, Germany, 23–26 April 2012.
26. Baffelli, S.; Frey, O.; Werner, C.; Hajnsek, I. System Characterization and Polarimetric Calibration of the Ku-Band Advanced Polarimetric Interferometer. In Proceedings of the 11th European Conference on Synthetic Aperture Radar, Hamburg, Germany, 6–9 June 2016; pp. 1–6.
27. Hecht, E. *Optics*, 4th ed.; Addison-Wesley: San Francisco, CA, USA, 2002; Volume 3.
28. Graham, L.C. Synthetic Interferometer Radar For Topographic Mapping. *Proc. IEEE* **1974**, *62*, 763–768.
29. Goldstein, R.M.; Zebker, H.A.; Werner, C.L. Satellite radar interferometry: Two-Dimensional phase unwrapping. *Radio Sci.* **1988**, *23*, 713–720.